Supporting Information:

High-Speed AFM Reveals Ligand-Dependent Supramolecular Switching of Human Phosphofructokinase-1

Shuangyu Luo[1], Arnav Patil[1], Nicholas Primanis-Erickson[1], Xiaoding Jiang[1], Bradley A Webb[2], Ku-Lung Hsu[1], Yi-Chih Lin[1,*]

[1] Department of Chemistry, The University of Texas at Austin, Austin, Texas 78712, USA
[2] Department of Biochemistry and Molecular Medicine, West Virginia University, Morgantown, West Virginia 26506, USA

*Correspondence to: Yi-Chih Lin (yichih.lin@utexas.edu)

Table of Contents

Experimental Methods:

Human PFKL protein and cryo-EM structures

Recombinant N-terminal His-tagged human PFKL WT (NP_002617) and PFKL N702T, were purified from Sf9 cells as reported previously.[1] The cryo-EM structure of R-state PFKL tetramer (PDB: 8W2G) and T-state PFKL tetramer (PDB: 8W2H) were collected from Protein Data Bank and illustrated by UCSF ChimeraX.[2-4]

HS-AFM Experiments

The basic imaging buffer consisted of 50 mM HEPES (pH 7.4), 2 mM $CaCl_2$, and 10 mM $MgCl_2$, supplemented with the indicated KCl concentration (100 mM or 300 mM). PFKL protein samples were either deposited onto freshly cleaved mica or introduced directly into the fluid cell of the HS-AFM for in situ assembly experiments.

All movies were acquired in amplitude modulation mode using a high-speed AFM (MS-NEX, RIBM Co., Ltd., Japan). Ultrashort cantilevers (NanoWorld, Switzerland) with spring constants of 0.15 or 0.6 $N \cdot m^{-1}$, resonance frequency of 0.6 MHz, and a quality factor of ~1.5 in buffer were used. Cantilevers were sharpened by oxygen plasma etching if needed. Tip–sample interactions were minimized by maintaining the set-point/free-amplitude ratio at ~0.85, with a free amplitude of ~1.0 nm. HS-AFM images were recorded at 1-5 frames/s.

HS-AFM Image Processing and Data Analysis

All HS-AFM images were processed in ImageJ[5]. Surface coverage and height histograms from HS-AFM frames were analyzed using ImageJ. Further quantitative analyses, including sigmoidal growth fitting and dissociation kinetics, were analyzed by custom routines in MATLAB R2024a. Simulated AFM images (4 pixels/nm resolution) were generated using a custom Python code by convolving the protein PDB structure with a cone-shape tip (tip radius 1 nm, cone angle 15°).

MD Simulations

The starting coordinates for all-atom molecular dynamics (MD) simulations were derived from the cryo-EM structure of the wild-type PFKL tetramer in the T-state (PDB: 8W2H)[1], with missing N-terminal residues 1-12 in each chain modeled using AlphaFold[6] and the N702T mutation performed with the PyMOL mutagenesis tool[7]. In this study, only APO structure was simulated, without ligands. To create the lattice model, six surrounding tetramers were positioned relative to the central tetramer to reproduce the observed lattice symmetry in HS-AFM (**Fig. 5C**). The initial edge-to-edge distance between adjacent tetramers was set to a minimum of 0.3 nm to avoid trapping the simulation in a local energy minimum caused by strong hydrogen bond formation. Throughout the analysis, tetramer nomenclature is as follows: T0 (or Tet 0) is the central tetramer, surrounded by 6 surrounding tetramers (Tet 1-Tet 6 or T1-T6). Tetramers 1 and 4, 2 and 5, and 3 and 6 were initially symmetry-related. Chains were named alphabetically within each tetramer, such that the first residue in the sequence would be Tetramer 0 Chain A Met 1 (T0A:M1).

Simulations were performed using the GROMACS software package (version 2024.2)[8]. The CHARMM36[9] force field was used to describe the protein and ions, and water molecules were modeled using the TIP3P model, which is the water model for which the CHARMM36 force field is parameterized[10]. The system was neutralized and solvated in a 150 mM KCl aqueous solution to mimic the imaging conditions and placed in a triclinic simulation box expanded to ensure a minimum distance of 2 nm between periodic images of protein molecules. The resulting box was composed of 3,307,506 atoms and enclosed a volume of 3.3×10^4 nm^3 (**Table S5**)

All simulations were performed using the leap-frog integrator[11] with a time-step of 2 fs. Bonds involving hydrogen atoms were constrained using the LINCS algorithm[12]. Short-range electrostatic and van der Waals interactions were truncated at 1.0 nm using a Verlet cutoff scheme. Long-range electrostatic interactions were computed using the particle mesh Ewald

(PME) method[13]. Long-range dispersion corrections were applied to both energy and pressure. Periodic boundary conditions were applied in all three dimensions.

Energy minimization was performed using the steepest descent algorithm in two stages. In the first stage, water molecules were allowed to relax while harmonic positional restraints were applied to protein heavy atoms. Following this, protein atoms were allowed to relax in the second stage to decrease the maximum force below 1000 kJ mol^{-1} nm^{-1}. Following minimization, the system was equilibrated using a multi-step process in which the force constants of harmonic position constraints were gradually decreased from 1000 kJ mol^{-1} nm^{-2} to 0 kJ mol^{-1} nm^{-2} to allow relaxation of the protein lattice within the solvent environment. The first two steps were performed in the NVT ensemble, while the latter four steps were performed in the NPT ensemble. More details regarding the system setup and equilibration process can be found in **Table S6**.

During production simulations, the temperature of the system was maintained at 310 K using the velocity-rescaling thermostat[14] with a time constant of 0.1 ps. Temperature coupling was applied separately to the protein and solvent components of the system. Pressure was maintained at 1.0 bar using the stochastic cell-rescaling barostat[15] with isotropic coupling and a time constant of 5 ps. A single production trajectory of 10 ns was generated. Atom positions and energies were saved every 10 ps. Prior to analysis, trajectories were processed in GROMACS to remove periodic boundary condition artifacts and then aligned translationally and rotationally to the initial structure. Structural analyses were performed using the MDAnalysis python package (version 2.10)[16,17]. The equilibrium portion of the trajectory, determined from stabilization of center-of-mass distances between neighboring tetramers and the central tetramer, as well as the RMSD from the initial post-equilibrium structure, corresponding to t = 2-4 ns of simulation time, was isolated for analysis. The lattice plane was defined based on the centers-of-mass of neighboring tetramers and recomputed on a per-frame basis to measure displacement in the lateral and normal directions relative to the plane. The plane was fit to the array of points with singular-value decomposition (SVD).

The potential for inter-protein contacts was predicted based on a threshold criterion of Cβ distances within 1.0 nm of each other[18]. The capability of electrostatic interactions was predicted on a per-residue basis by determining whether a residue pair had opposite charges. The potential for a hydrogen bond was predicted solely based on hydrogen bond donor-acceptor identities present in side chains. For further analysis, residues forming a persistent contact in each simulation were defined as being within the threshold distance for at least 25% of the surveyed frames.

All production simulations were performed on the Texas Advanced Computing Center (TACC) Lonestar6 high-performance computing cluster.

References:

1. Lynch, E.M. et al. Structural basis for allosteric regulation of human phosphofructokinase-1. *Nature Communications* **15**, 7323 (2024).
2. Goddard, T.D. et al. UCSF ChimeraX: Meeting modern challenges in visualization and analysis. *Protein Science* **27**, 14–25 (2018).
3. Pettersen, E.F. et al. UCSF ChimeraX: Structure visualization for researchers, educators, and developers. *Protein Science* **30**, 70–82 (2021).
4. Meng, E.C. et al. UCSF ChimeraX: Tools for structure building and analysis. *Protein Science* **32**, e4792 (2023).
5. Schneider, C.A., Rasband, W.S. & Eliceiri, K.W. NIH Image to ImageJ: 25 years of image analysis. *Nature Methods* **9**, 671–675 (2012).
6. Jumper, J. et al. Highly accurate protein structure prediction with AlphaFold. *Nature* **596**, 583–589 (2021).
7. Schrödinger, L.L.C. The PyMOL Molecular Graphics System, Version 3.0. (2015).
8. Abraham, M.J. et al. GROMACS: High performance molecular simulations through multi-level parallelism from laptops to supercomputers. *SoftwareX* **1-2**, 19–25 (2015).
9. Huang, J. & MacKerell, A.D. CHARMM36 all-atom additive protein force field: validation based on comparison to NMR data. *J Comput Chem* **34**, 2135–45 (2013).
10. Jorgensen, W.L., Chandrasekhar, J., Madura, J.D., Impey, R.W. & Klein, M.L. Comparison of Simple Potential Functions for Simulating Liquid Water. *Journal of Chemical Physics* **79**, 926–935 (1983).
11. Hockney, R.W., Goel, S.P. & Eastwood, J.W. Quiet high-resolution computer models of a plasma. *Journal of Computational Physics* **14**, 148–158 (1974).
12. Hess, B., Bekker, H., Berendsen, H.J.C. & Fraaije, J.G.E.M. LINCS: A linear constraint solver for molecular simulations. *Journal of Computational Chemistry* **18**, 1463–1472 (1997).
13. Darden, T., York, D. & Pedersen, L. Particle Mesh Ewald - an N.Log(N) Method for Ewald Sums in Large Systems. *Journal of Chemical Physics* **98**, 10089–10092 (1993).
14. Bussi, G., Donadio, D. & Parrinello, M. Canonical sampling through velocity rescaling. *The Journal of Chemical Physics* **126**, 014101 (2007).
15. Bernetti, M. & Bussi, G. Pressure control using stochastic cell rescaling. *The Journal of Chemical Physics* **153**, 114107 (2020).
16. Gowers, R.J. et al. MDAnalysis: A Python Package for the Rapid Analysis of Molecular Dynamics Simulations. *SciPy 2016* (2016).
17. Michaud-Agrawal, N., Denning, E.J., Woolf, T.B. & Beckstein, O. MDAnalysis: A Toolkit for the Analysis of Molecular Dynamics Simulations. *Journal of computational chemistry* **32**, 2319–2327 (2011).
18. Monastyrskyy, B., D'Andrea, D., Fidelis, K., Tramontano, A. & Kryshtafovych, A. Evaluation of residue-residue contact prediction in CASP10. *Proteins* **82**, 138–153 (2014).

Supplementary Tables:

Table S1. HS-AFM Experimental Conditions for PFKL WT

Figures	Dynamics	Molecular players			Imaging buffer			Protein Deposition	
		WT (nM)	F6P (mM)	ATP (mM)	KCl (mM)	Mg^{2+} (mM)	Ca^{2+} (mM)	Mica incubation (min)	Live addition
2A	Lattice-like Assembly	225			300	10	2		V
2B	Lattice-like Assembly	225		1	300	10	2		V
2E	(i) Filament Assembly	255	2 (2^{nd})	1(1^{st})	300	10	2		V
	(ii) Lattice-like Assembly	170	2 (1^{st})	1 (2^{nd})	300	10	2		V
2F	Filament Assembly	225	2	5	300	10	2		V
2G	(left) Network Geometry	255	2	1	300	10	2		V
	(right) Linear Geometry	425	2	1	300	10	2		V
2H	Linearized Filament	425	2	1	300	10	2		V
	Kinked Filament	425	2	1	300	10	2		V
S2A	Self-Assembly	225			300	10	2		V
S2B	Self-Assembly	225		1	300	10	2		V
S2C	Self-Assembly	225		5	300	10	2		V
S3A	Disassociation	225		5	300	10	2		V
S4A	(i) Filament Assembly	170	2 (2^{nd})	1 (1^{st})	300	10	2		V
	(ii) Filament Assembly	425	2 (2^{nd})	1 (1^{st})	300	10	2		V
S4B	Filament Assembly	170	2 (2^{nd})	1 (1^{st})	300	10	2		V
S4C	Filament Assembly	225	2	5	300	10	2		V
S5A	Filament Assembly (Network)	255	2	1	300	10	2		V
S5B	Filament Assembly (Linear)	425	2	1	300	10	2		V
3A	Single Molecular Characterization	225			100	10	2		V
3B	Membrane Interaction	270			100	10	2	5	
		1000			100	10	2	3	
		3000			100	10	2	5	
3D	Membrane Interaction	3000			100	10	2	5	

Table S1. HS-AFM Experimental Conditions for PFKL WT (continued)

Figures	Dynamics	Molecular players			Imaging buffer			Protein Deposition	
		WT (nM)	F6P (mM)	ATP (mM)	KCl (mM)	Mg^{2+} (mM)	Ca^{2+} (mM)	Mica incubation (min)	Live addition
S6A	Single Molecular Characterization	225→270			100	10	2		V
S6B	Membrane Interaction	2700			100	10	2	1	
S6C-D	Membrane Interaction	1000			100	10	2	3	
S6E-F	Membrane Interaction	3000			100	10	2	5	

Table S2. HS-AFM Experimental Conditions for PFKL N702T

Figures	Dynamics	Molecular players			Imaging buffer			Protein Deposition	
		N702T (nM)	F6P (mM)	ATP (mM)	KCl (mM)	Mg^{2+} (mM)	Ca^{2+} (mM)	Mica incubation (min)	Live addition
4A	Lattice Dissociation	100			100		2	10	
4C*	Self-Assembly	300			300		2		V
4D	Self-Assembly	300			100		2		V
		800			100		2		V
		300			300		2		V
4E	Self-Assembly	300			20		2		V
5A-B	(i) 2D Lattice Formation	90			300	10	2		V
5A-B	(ii) 2D Lattice Formation	90		1	300	10	2		V
5A-B	(iii) 2D Lattice Formation	170	2	1	300	10	2		V
5E	Lattice Dissociation	100			100		2	10	
S7A	Self-Assembly	100			100		2	3	
		100			100		2	10	
		500			100		2	5	
		500			100		2	10	
		500			100		2	15	
		300			20		2	10	
		300			300		2	10	
S8A	Self-Assembly	300			20		2		V
S8B	(i) Self-Assembly	800			100		2		V
	(ii) Self-Assembly	300			100		2		V
S8C	Self-Assembly	300			300		2		V
S8D	(i) Self-Assembly	300			20		2		V
	(ii) Self-Assembly	300			100		2		V

*: After full lattice coverage had formed on mica, 2 mM F6P was added at 77 min, followed by 1 mM ATP at 93 min.

Table S3. Summary of Sigmoidal Fitting Parameters for Lattice Growth

Figures	Dynamics	PFKL	Functional state	Experiment condition		Baseline (%)	Hill Coefficient	Half Time ($t_{1/2}$, min)	Top (%)
				Protein (nM)	KCl (mM)				
2D	Self-Assembly	WT	APO	225	300	N.A. (linear fit)			
		WT	+1 mM ATP	225	300	0	4.4	60.9	100
		WT	+5 mM ATP	225	300	0	4.9	55.9	100
4C*	Self-Assembly	N702T	APO	300	300	3.8	5.0	36.3	95.8
4D	Self-Assembly	N702T	APO	300	100	4.7	3.5	46.1	100
		N702T	APO	800	100	0.4	6.1	31.6	94.5

*: During the final stage of imaging, 2 mM F6P (77 min) and 1 mM ATP (93 min) were sequentially added.

Table S4. PFKL Lattice Dissociation Kinetics

Figures	Dynamics	PFKL	Experiment conditions		Amplitude	k	Half Time
			Protein (nM)	KCl (mM)			
S3B	Dissociation (5 mM ATP)	WT	225	300	77.00%	0.1957 s^{-1}	3.5 s
4B (bottom)	Dissociation	N702T	100	100	57.13%	0.0148 s^{-1}	46.7 s

Table S5. Experimental Setups for Molecular Dynamics (MD) simulations

System (PFKL N702T)	Box Volume (nm^3)	Total Atoms	Protein Atoms	Water Molecules	KCl concentration (mM)
PFKL N702T Lattice (Seven Tetramers)	33415.2	3307506	334180	989758	150

Table S6. Equilibration Protocol for MD Simulations

Step	Ensemble	Length (ps)	Time Step (fs)	Harmonic Restraint Force Constant (kJ mol^{-1} nm^{-2})
1	NVT	100	2	1000
2	NVT	100	2	250
3	NPT	100	1	250
4	NPT	200	1	50
5	NPT	400	2	10
6	NPT	100	2	0

Table S7. Inter-tetramer Interactions with Central Dimer in MD Simulation (from 2 ns to 4 ns)

Edge Tetramer (Tetramer-Chain)		Central Tetramer (Tetramer-Chain)		Contact Type		Contact Frequency	Distance (Å)	
Chain ID	Residue	Chain ID	Residue	Electrostatic	Hydrogen Bond		Mean	SD
T1A	LYS395	T0C	GLY697	FALSE	FALSE	59	8.94	0.63
T1A	GLU396	T0C	LYS696	TRUE	N-H..O	150	7.38	1.38
T1A	GLU396	T0C	GLY697	FALSE	FALSE	184	7.39	1.03
T1A	LYS397	T0C	LYS696	FALSE	FALSE	142	7.33	1.61
T1A	LYS397	T0C	GLY697	FALSE	FALSE	125	7.65	2
T1A	LYS397	T0C	ARG698	FALSE	FALSE	59	8.01	0.94
T1A	SER398	T0C	LYS696	FALSE	N-H..O	93	8.56	1.23
T1A	SER398	T0C	GLY697	FALSE	FALSE	154	8.23	1.08
T1A	SER398	T0C	ARG698	FALSE	FALSE	77	9.21	0.55
T1A	ASN399	T0C	GLU515	FALSE	N-H..O	58	9.44	0.41
T1A	ASN399	T0C	LYS696	FALSE	N-H..O	145	7.6	1.3
T1A	ASN399	T0C	GLY697	FALSE	FALSE	127	7.52	1.27
T1A	ASN399	T0C	ARG698	FALSE	FALSE	169	8.24	0.98
T1A	TYR694	T0C	ARG485	FALSE	FALSE	76	9.34	0.49
T1A	ARG695	T0C	GLU482	TRUE	FALSE	89	9.2	0.59
T1A	ARG695	T0C	ARG485	FALSE	FALSE	116	8.89	0.64
T1A	LYS696	T0C	GLU478	TRUE	N-H..O	167	8.97	0.72
T1A	LYS696	T0C	VAL481	FALSE	FALSE	127	9.04	0.48
T1A	LYS696	T0C	GLU482	TRUE	N-H..O	198	7.62	0.72
T1A	LYS696	T0C	ARG485	FALSE	FALSE	167	8.43	1.01
T1A	GLY697	T0C	VAL481	FALSE	FALSE	150	9.19	0.46
T1A	GLY697	T0C	GLU482	FALSE	FALSE	146	8.89	0.66
T1A	GLY697	T0C	ARG485	FALSE	FALSE	196	7.41	1.05
T1A	GLY697	T0C	TYR514	FALSE	FALSE	50	9.48	0.41
T1A	GLY697	T0C	GLU515	FALSE	FALSE	136	8.61	0.86
T1A	GLY697	T0C	GLU516	FALSE	FALSE	154	8.78	0.58
T2C	GLY143	T0A	GLY62	FALSE	FALSE	52	8.76	0.95
T2D	MET1	T0B	ASP5	FALSE	FALSE	106	8.33	1.08
T2D	MET1	T0B	LYS8	FALSE	FALSE	179	7.57	1.44
T2D	MET1	T0B	LEU9	FALSE	FALSE	91	8.46	0.91
T2D	MET1	T0B	SER12	FALSE	FALSE	90	8.05	1.25
T2D	ALA2	T0B	ASP5	FALSE	FALSE	71	8.18	1.06
T2D	ALA2	T0B	LYS8	FALSE	FALSE	80	7.73	1.55
T2D	GLU326	T0B	ASP330	FALSE	FALSE	108	8.42	0.94
T2D	ALA327	T0B	ASP330	FALSE	FALSE	81	9.22	0.55
T2D	THR328	T0B	THR328	FALSE	FALSE	69	9.06	0.63
T2D	THR328	T0B	PRO329	FALSE	FALSE	115	9.13	0.66
T2D	THR328	T0B	ASP330	FALSE	FALSE	196	6.48	1.56
T2D	THR328	T0B	THR331	FALSE	FALSE	114	8.56	1.08
T2D	THR328	T0B	PRO332	FALSE	FALSE	50	9.31	0.52
T2D	PRO329	T0B	ASP330	FALSE	FALSE	115	9.06	0.66
T2D	ASP330	T0B	ASP330	FALSE	FALSE	116	7.59	1.26
T2D	ASP330	T0B	THR331	FALSE	FALSE	50	9.19	0.59
T2D	ASP330	T0B	PRO332	FALSE	FALSE	61	8.93	0.63
T2D	THR331	T0B	ASP330	FALSE	FALSE	118	7.86	1.12
T2D	GLU767	T0B	ARG151	TRUE	FALSE	65	9.42	0.48
T2D	HIS768	T0B	GLU137	TRUE	N-H..O	65	9.27	0.52
T2D	THR770	T0B	GLU147	FALSE	FALSE	53	9.33	0.5
T2D	ARG772	T0B	GLU147	TRUE	FALSE	69	8.76	0.93
T3C	MET1	T0A	GLU724	FALSE	FALSE	148	8.45	0.9
T3C	MET1	T0A	LYS727	FALSE	FALSE	95	9.15	0.59
T3C	VAL4	T0A	THR702	FALSE	FALSE	67	9.16	0.61
T3C	VAL4	T0A	ALA703	FALSE	FALSE	186	8.21	1.05
T3C	VAL4	T0A	PRO704	FALSE	FALSE	200	6.26	0.49
T3C	VAL4	T0A	ASP705	FALSE	FALSE	91	9.06	0.61
T3C	VAL4	T0A	PRO721	FALSE	FALSE	160	9.32	0.43
T3C	VAL4	T0A	THR723	FALSE	FALSE	194	8.35	0.7
T3C	VAL4	T0A	GLU724	FALSE	FALSE	170	8.9	0.63
T3C	ASP5	T0A	PRO704	FALSE	FALSE	110	8.88	0.63
T3C	ASP5	T0A	GLU724	FALSE	FALSE	80	9.29	0.34

T3C	GLU7	T0A	THR702	FALSE	FALSE	54	9.34	0.5
T3C	GLU7	T0A	ALA703	FALSE	FALSE	129	8.97	0.63
T3C	GLU7	T0A	PRO704	FALSE	FALSE	85	9.44	0.43
T3C	LYS8	T0A	ALA703	FALSE	FALSE	163	8.49	0.98
T3C	LYS8	T0A	PRO704	FALSE	FALSE	114	8.76	0.74
T3C	LYS8	T0A	ASP705	TRUE	N-H..O	85	9.48	0.36
T3C	ALA11	T0A	ALA703	FALSE	FALSE	89	9.13	0.57
T3C	GLN372	T0A	HIS768	FALSE	N-H..N	71	9.03	0.6
T3C	ALA703	T0A	VAL4	FALSE	FALSE	56	9.13	0.72
T3C	PRO704	T0A	MET1	FALSE	FALSE	80	8.62	0.96
T3C	PRO704	T0A	ALA3	FALSE	FALSE	77	8.87	0.69
T3C	PRO704	T0A	VAL4	FALSE	FALSE	57	9.14	0.64
T3C	ASP705	T0A	MET1	FALSE	FALSE	96	8.7	0.84
T3C	ASP705	T0A	VAL4	FALSE	FALSE	84	8.6	0.58
T3C	PRO721	T0A	MET1	FALSE	FALSE	61	9.24	0.5
T3C	GLU724	T0A	MET1	FALSE	FALSE	52	9.2	0.53
T3C	HIS768	T0A	ARG772	FALSE	FALSE	138	9.38	0.41
T3C	HIS768	T0A	ASP777	TRUE	N-H..O	161	8.42	0.68
T3C	HIS768	T0A	LYS778	FALSE	N-H..N	82	8.83	0.81
T3C	HIS768	T0A	GLY779	FALSE	FALSE	111	8.57	0.99
T3C	THR770	T0A	THR770	FALSE	FALSE	183	8.04	0.76
T3C	THR770	T0A	ARG771	FALSE	FALSE	130	8.41	1.01
T3C	THR770	T0A	ARG772	FALSE	FALSE	175	7.69	1.08
T3C	THR770	T0A	ASP777	FALSE	FALSE	134	7.88	1.11
T3C	ARG771	T0A	GLU767	TRUE	FALSE	113	9.38	0.43
T3C	ARG771	T0A	HIS768	FALSE	FALSE	145	9.11	0.47
T3C	ARG771	T0A	THR770	FALSE	FALSE	147	7.64	1.31
T3C	ARG771	T0A	ARG771	FALSE	FALSE	70	8.86	0.59
T3C	ARG771	T0A	ARG772	FALSE	FALSE	88	8.99	0.52
T3C	ARG772	T0A	THR770	FALSE	FALSE	87	9.26	0.58
T3C	ARG772	T0A	ARG772	FALSE	FALSE	85	9.07	0.6
T3C	ASP777	T0A	GLU767	FALSE	FALSE	67	8.37	0.5
T3C	LYS778	T0A	GLU767	TRUE	N-H..O	56	9.33	0.52
T4C	ILE486	T0A	LYS696	FALSE	FALSE	125	9.07	0.55
T4C	GLY488	T0A	LYS696	FALSE	FALSE	110	8.87	0.78
T4C	GLY488	T0A	GLY697	FALSE	FALSE	128	8.95	0.72
T4C	LYS696	T0A	ILE486	FALSE	FALSE	81	8.19	1.64
T4C	LYS696	T0A	GLY488	FALSE	FALSE	89	8.79	0.78
T4C	GLY697	T0A	ASN399	FALSE	FALSE	112	9.03	0.7
T4C	GLY697	T0A	GLY488	FALSE	FALSE	92	8.74	1.02
T5B	MET1	T0D	MET1	FALSE	FALSE	107	7.81	1.1
T5B	MET1	T0D	ALA2	FALSE	FALSE	57	7.13	2.02
T5B	MET1	T0D	VAL4	FALSE	FALSE	68	8.28	1.13
T5B	ALA2	T0D	MET1	FALSE	FALSE	124	8.47	0.95
T5B	ALA2	T0D	ALA2	FALSE	FALSE	55	8.78	1.18
T5B	ASP5	T0D	MET1	FALSE	FALSE	143	7.15	1.47
T5B	ASP5	T0D	ALA2	FALSE	FALSE	58	8.02	1.39
T5B	LYS8	T0D	MET1	FALSE	FALSE	72	8.54	0.9
T5B	LEU9	T0D	MET1	FALSE	FALSE	56	8.05	1.17
T5B	ARG129	T0D	ASP330	TRUE	FALSE	91	9.57	0.34
T5B	SER130	T0D	PRO329	FALSE	FALSE	76	9.41	0.43
T5B	SER130	T0D	ASP330	FALSE	O-H..O	200	7.22	0.73
T5B	GLY133	T0D	ASP330	FALSE	FALSE	85	9.2	0.53
T5B	HIS155	T0D	ASP330	TRUE	N-H..O	70	9.31	0.44
T5B	PRO329	T0D	THR328	FALSE	FALSE	142	9.18	0.51
T5B	PRO329	T0D	ASP330	FALSE	FALSE	87	9.29	0.5
T5B	ASP330	T0D	GLU326	FALSE	FALSE	200	6.82	0.73
T5B	ASP330	T0D	ALA327	FALSE	FALSE	193	8.85	0.49
T5B	ASP330	T0D	THR328	FALSE	FALSE	200	5.76	0.59
T5B	ASP330	T0D	ASP330	FALSE	FALSE	174	8.56	0.86
T5B	ASP330	T0D	THR331	FALSE	FALSE	198	7.84	0.65
T5B	ASP330	T0D	LEU766	FALSE	FALSE	128	9.29	0.51
T5B	THR331	T0D	THR328	FALSE	FALSE	187	8.85	0.4
T5B	PRO332	T0D	THR328	FALSE	FALSE	200	8.02	0.75
T5B	PRO332	T0D	PRO329	FALSE	FALSE	148	8.96	0.78
T5B	PRO332	T0D	ASP330	FALSE	FALSE	71	8.79	0.81

T5B	MET349	T0D	PRO329	FALSE	FALSE	176	8.72	0.65
T5B	MET349	T0D	ASP330	FALSE	FALSE	63	9.55	0.36
T5B	GLU350	T0D	ARG151	TRUE	FALSE	200	8.41	0.57
T5B	GLU350	T0D	SER154	FALSE	O-H..O	98	9.32	0.43
T5B	GLN353	T0D	ARG151	FALSE	FALSE	200	7.62	0.46
T5B	GLN353	T0D	SER154	FALSE	O-H..O	142	9.39	0.36
T5B	MET354	T0D	THR148	FALSE	FALSE	67	9.73	0.22
T5B	MET354	T0D	ARG151	FALSE	FALSE	196	8.62	0.53
T5B	GLU357	T0D	GLU147	FALSE	FALSE	185	8.64	0.66
T5B	GLU357	T0D	THR148	FALSE	FALSE	66	9.64	0.27
T5B	GLU357	T0D	ARG151	TRUE	FALSE	165	9.15	0.46
T5B	LYS360	T0D	GLU147	TRUE	N-H..O	66	9.49	0.4
T5B	GLU369	T0D	GLU147	FALSE	FALSE	61	9.34	0.4
T5B	GLU765	T0D	LYS8	TRUE	N-H..O	158	9.43	0.41
T5B	HIS768	T0D	ALA11	FALSE	FALSE	125	8.73	0.91
T5B	HIS768	T0D	ALA14	FALSE	FALSE	112	8.89	0.85
T5B	HIS768	T0D	GLY15	FALSE	FALSE	108	9.21	0.57
T5B	VAL769	T0D	ARG151	FALSE	FALSE	101	9.4	0.51
T5B	VAL769	T0D	THR152	FALSE	FALSE	90	9.24	0.6
T5B	ARG771	T0D	THR148	FALSE	FALSE	200	7.45	0.63
T5B	ARG771	T0D	ARG151	FALSE	FALSE	51	9.62	0.29
T5B	ARG771	T0D	THR152	FALSE	FALSE	174	8.96	0.63
T5B	LEU774	T0D	THR148	FALSE	FALSE	166	9.01	0.64
T5B	LEU774	T0D	ARG151	FALSE	FALSE	136	9.13	0.54
T5B	MET776	T0D	SER146	FALSE	FALSE	53	9.53	0.41
T5B	MET776	T0D	GLU147	FALSE	FALSE	84	9.54	0.32
T5B	MET776	T0D	THR148	FALSE	FALSE	200	6.37	0.71
T5B	MET776	T0D	ARG151	FALSE	FALSE	124	9.18	0.53
T5B	MET776	T0D	THR152	FALSE	FALSE	63	9.56	0.31
T5B	ASP777	T0D	THR148	FALSE	FALSE	138	9.26	0.44
T6A	THR770	T0C	THR770	FALSE	FALSE	64	9.08	0.66
T6A	THR770	T0C	ARG771	FALSE	FALSE	94	8.95	0.7
T6A	ARG771	T0C	THR770	FALSE	FALSE	58	8.73	0.63
T6A	ARG771	T0C	ARG771	FALSE	FALSE	53	9.02	0.56
T6A	ARG772	T0C	THR770	FALSE	FALSE	69	8.62	0.86
T6A	ASP777	T0C	HIS768	TRUE	N-H..O	148	8.89	0.68
T6A	ASP777	T0C	THR770	FALSE	FALSE	62	7.98	0.86
T6A	LYS778	T0C	HIS768	FALSE	N-H..N	175	7.77	1.7
T6A	LYS778	T0C	THR770	FALSE	FALSE	51	8.6	0.4
T6A	GLY779	T0C	HIS768	FALSE	FALSE	50	8.77	0.64
T6A	PHE780	T0C	HIS768	FALSE	FALSE	90	8.28	1.27

Note: The colored zones highlight spatial contacts within local interfaces between adjacent tetramers in the MD simulations. Each color corresponds to a zoomed-in structural view shown in **Fig. 6** and **Fig. S10**.

231

Supplementary Figures:

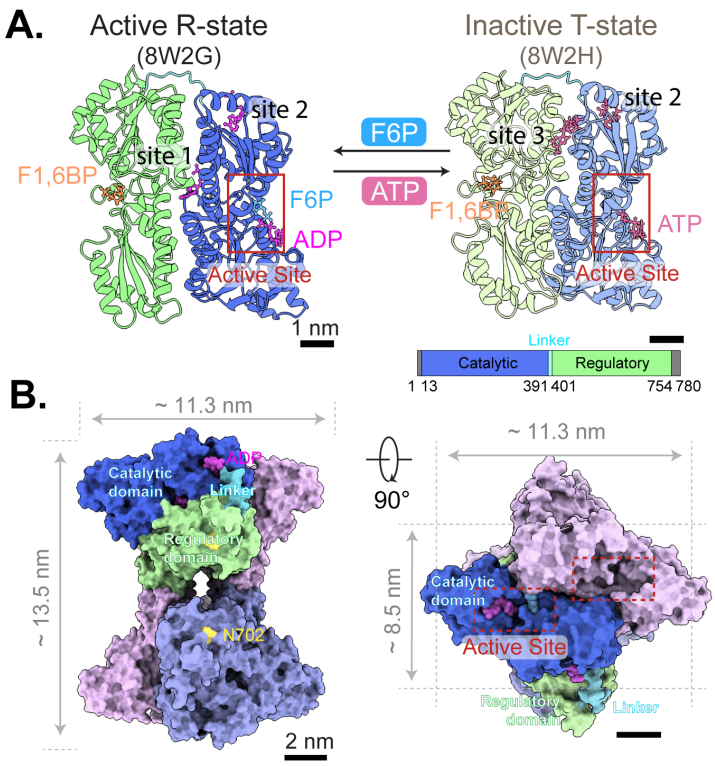

Figure S1. Architectures of PFKL from monomeric form to tetramer. (A) Monomeric structures of PFKL in its active R-state (PDB: 8W2G; with F1,6BP, F6P, and ADP) and inactive T-state (PDB: 8W2H; with F1,6BP and ATP). PFKL is involved in catalyzing the phosphorylation of F6P to F1,6BP with ATP hydrolysis at active site (red rectangle). **(B)** PFKL tetramer in the active R-state (PDB: 8W2G). With 90 degrees of rotation, the extrusions of PFKL tetramer show a dimension of ~11.3 nm and ~8.5 nm, with two active sites. Within one of the monomers, the catalytic domain (dark blue), interdomain linker (light blue), and regulatory domain (purple) are highlighted, respectively. The N702 residue (yellow) is crucial to form filamentous structures.

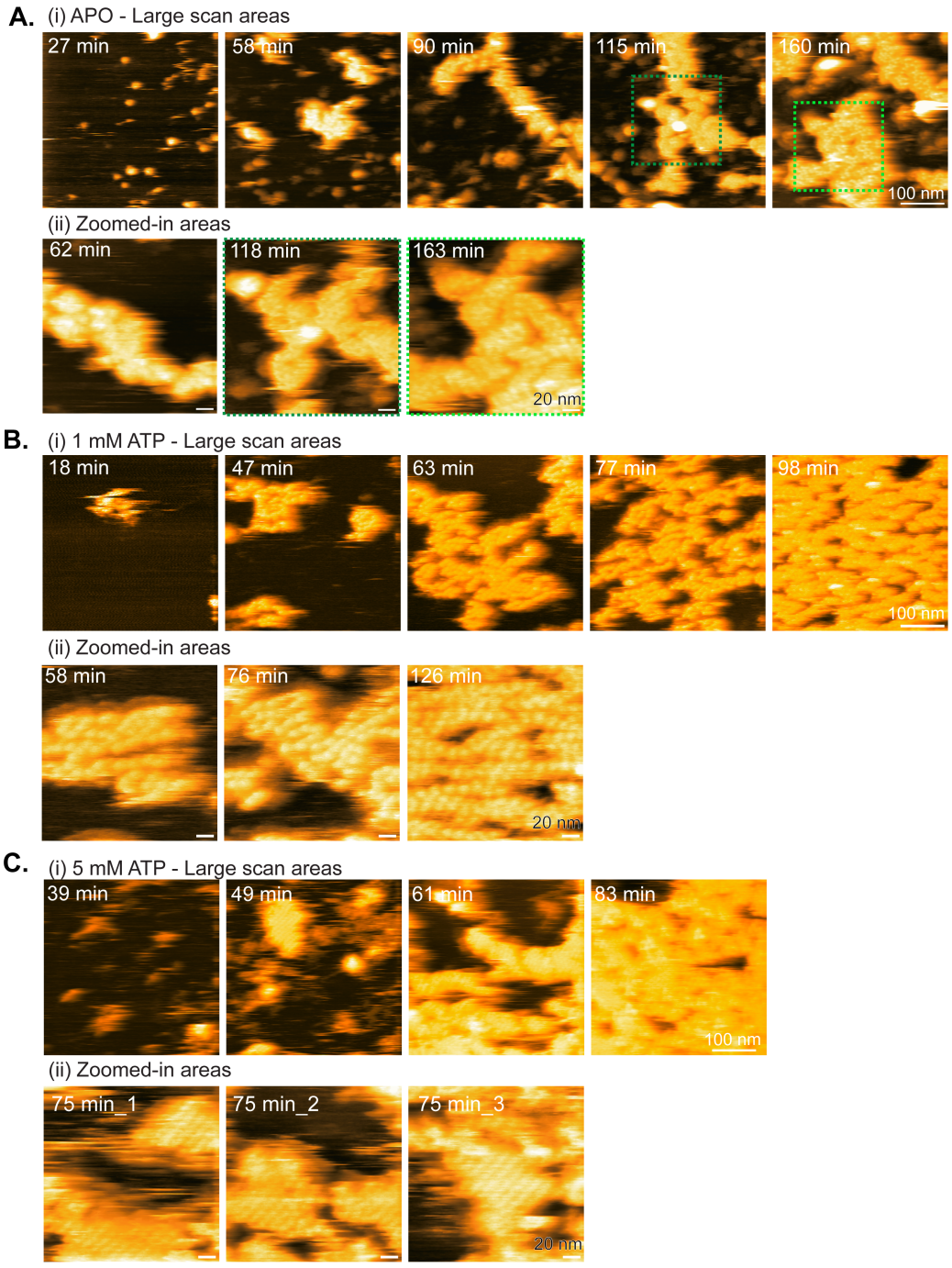

Figure S2. Time-lapse HS-AFM imaging of PFKL WT lattice-like assembly under APO and ATP conditions. (A-C) Representative HS-AFM images showing PFKL WT (225 nM) self-assembling into lattice-like assemblies in buffer containing 300 mM KCl under APO, 1 mM ATP, or 5 mM ATP conditions. Lattice-like domains progressively expand over time, with ATP-treated conditions showing more cooperative growth of ordered two-dimensional assemblies.

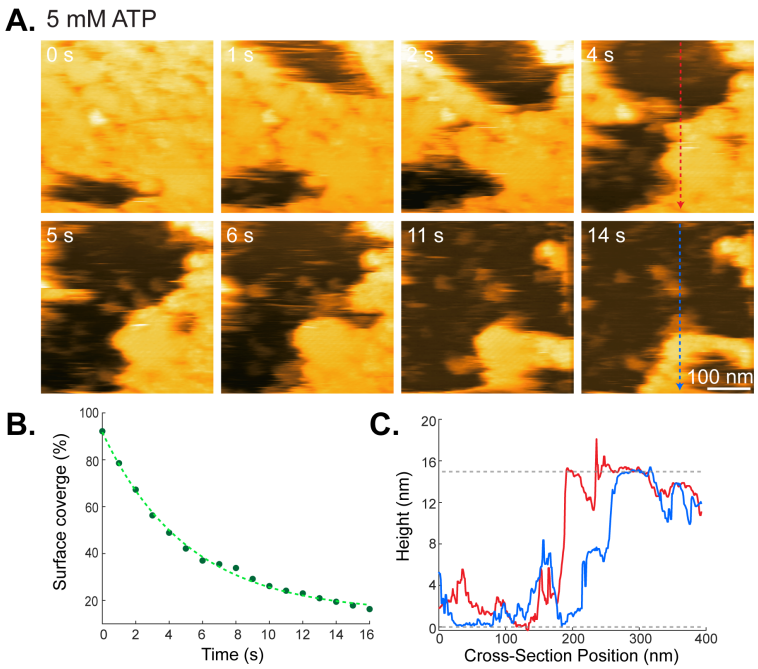

Figure S3. Dissociation kinetics of ATP-treated PFKL WT lattice-like assemblies during HS-AFM imaging. (A) Time-lapse HS-AFM images showing dissociation of the PFKL WT lattice-like assembly (225 nM protein in buffer containing 300 mM KCl and 5 mM ATP) during HS-AFM scanning. **(B)** Quantification of lattice dissociation based on surface coverage analysis, fitted with an exponential decay yielding a halftime of 3.5 s. **(C)** Representative cross-sectional height profiles across the mica substrate and the PFKL WT lattice-like assembly.

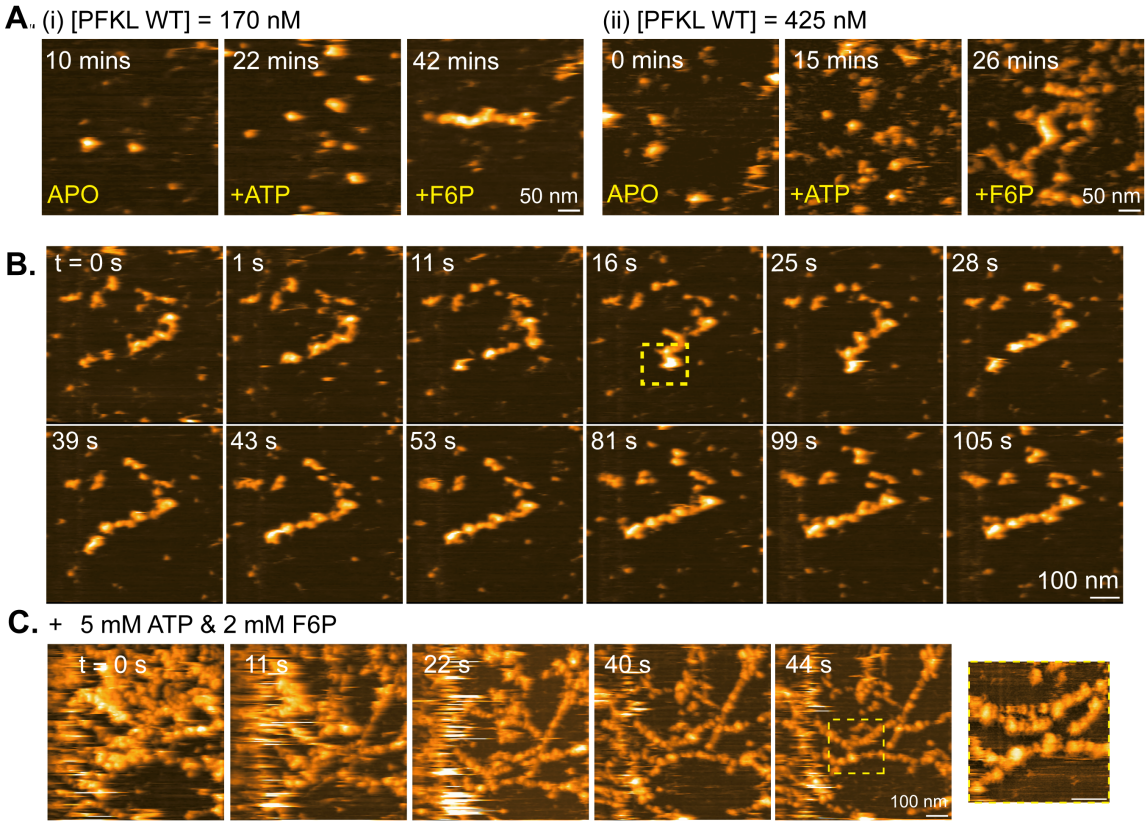

Figure S4. PFKL WT self-assembles into filamentous structures upon F6P treatment. **(A)** With a short incubation time on mica, PFKL WT formed small protein aggregates in both APO and ATP conditions. However, after adding 2 mM F6P into the 300mM KCl imaging buffer, PFKL WT self-assembled into filamentous structures, regardless of the (i) absence or presence of Mg^{2+} ions. **(B)** Real-time HS-AFM imaging of PFKL WT (170 nM) showing filament formation after sequential addition of ATP and F6P in buffer containing 300 mM KCl. The resulting filaments remained stable during imaging without detectable dissociation. **(C)** Real-time observation of PFKL WT filament formation in the presence of 5 mM ATP and 2 mM F6P.

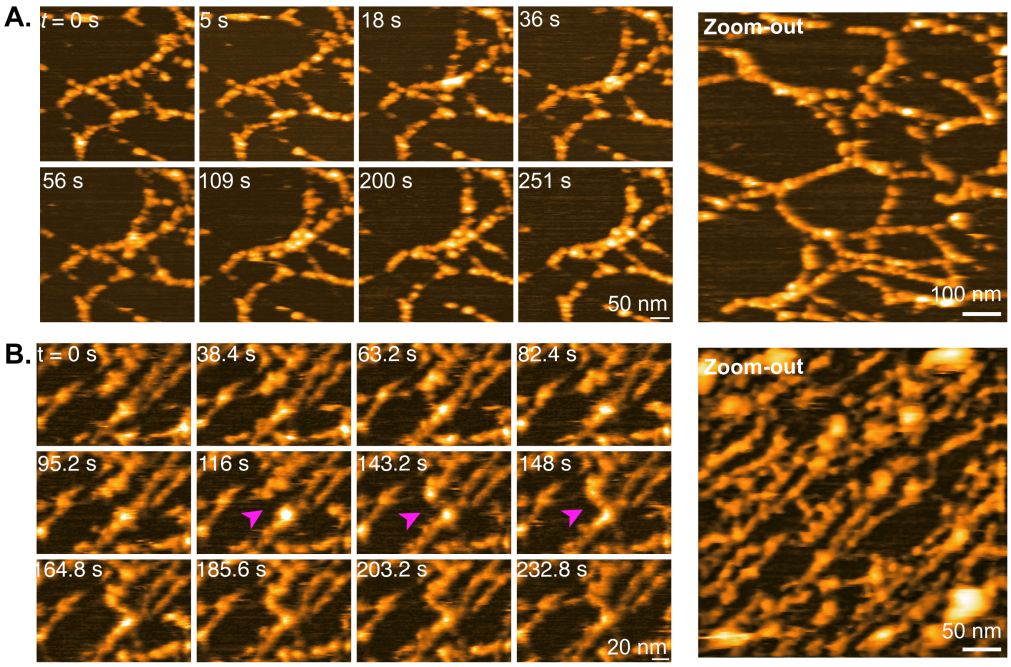

Figure S5. PFKL WT filamentous structures in the presence of ATP and F6P. (A-B) Real-time observations of PFKL WT filaments in network-like (protein concentration: 255 nM) and linear (protein concentration: 425 nM) geometry. During the observation, individual PFKL WT building blocks (tetramer or dimer of tetramers) exhibited dynamic movements and could locally form new filamentous connections (magenta arrows in **B**), but the overall filament architecture stayed unchanged**.**

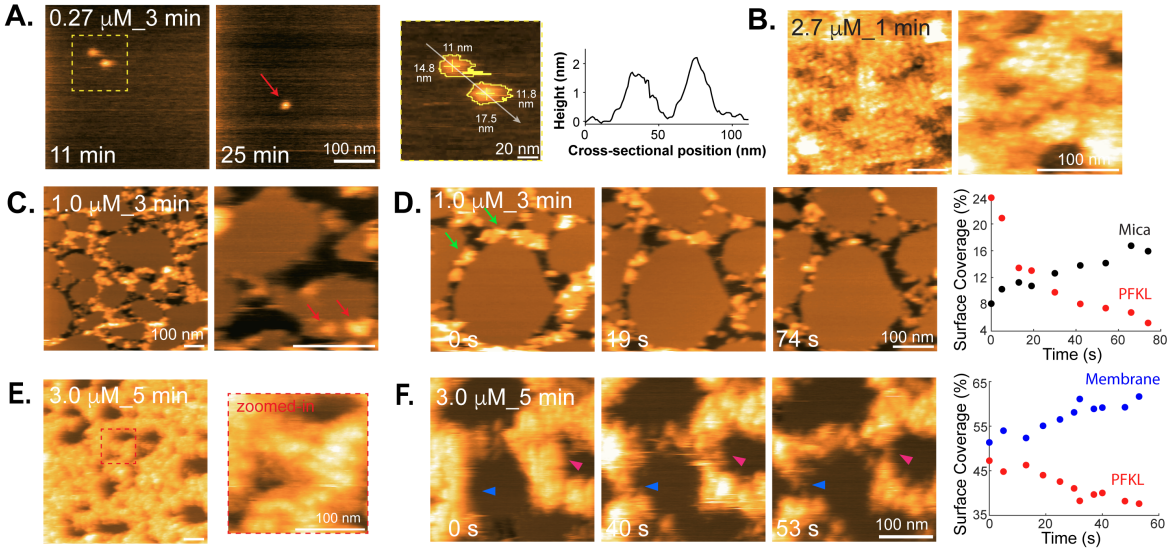

Figure S6. PFKL binding and self-assembly on continuous membranes and membrane patches. (A-B) Time-lapse HS-AFM images of APO-PFKL WT in 100 mM KCl buffer deposited onto a continuous, supported lipid bilayer (DOPC/DOPS=3/2). Insets indicate protein concentration and the pre-incubation time on the membrane (experimental conditions summarized in **Table S1**). At low protein concentration (0.27 μM), individual PFKL tetramers were observed bound to the membrane. At higher concentration (2.7 μM), APO-PFKL WT assembled into lattice-like assemblies on the membrane surface. **(C-F)** Time-lapse HS-AFM images of APO-PFKL WT in 100 mM KCl buffer deposited onto preformed membrane patches on mica. **(C, E)** Zoomed-out and zoomed-in views showing varied densities of PFKL WT localized on or adjacent to membrane patches. **(D, F)** Real-time observation of PFKL WT lattice dissociation at inter-patch gaps. Right panels: Quantitative analysis of surface coverage, distinguishing PFKL assemblies from mica or membrane background.

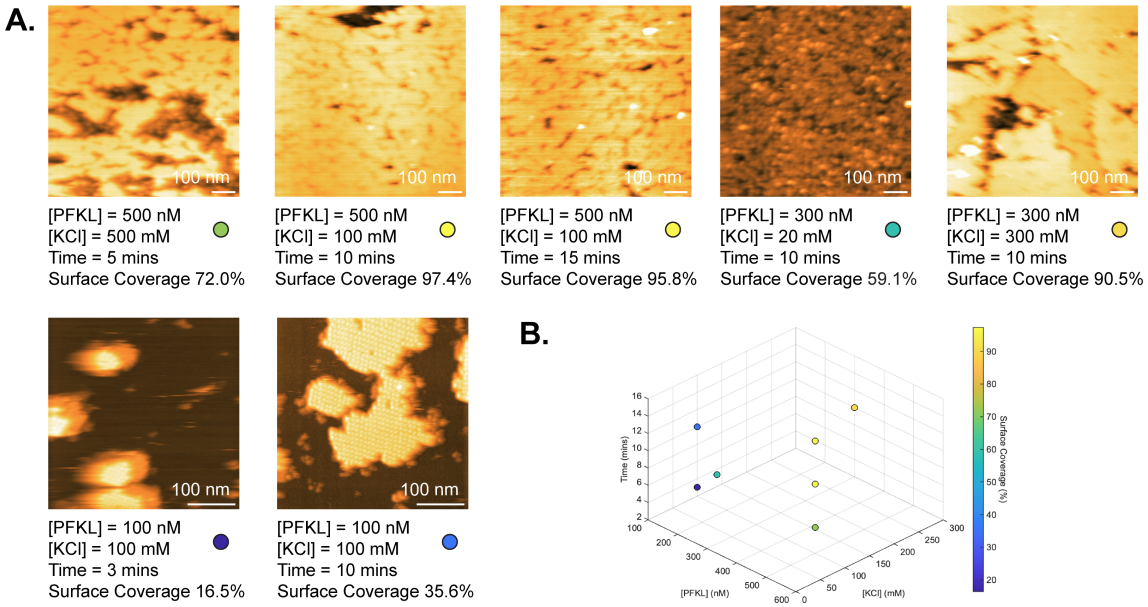

Figure S7. PFKL N702T self-assembles into highly ordered double-layer 2D lattice under varied experimental conditions. (A) Representative HS-AFM images of PFKL N702T 2D lattice formed on freshly cleaved mica at different protein and KCl concentrations and incubation times. When the KCl concentration was lowered to 20 mM, PFKL N702T self-assembled into relatively disorganized structures. **(B)** Surface coverage of PFKL N702T lattice as a function of protein concentration, incubation time, and KCl concentration, where the color represents the measured surface coverage percentage.

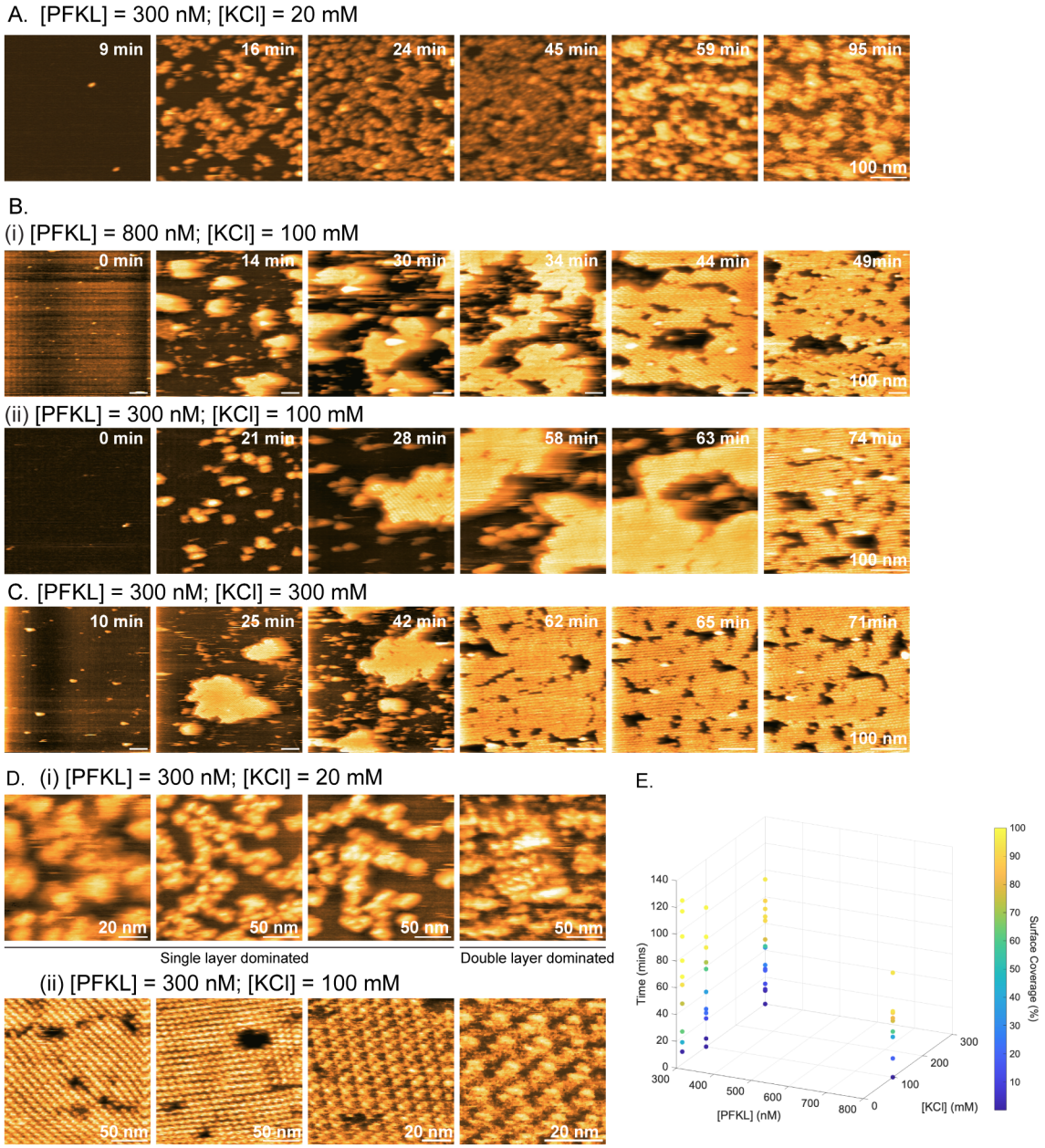

Figure S8. Self-assembly of PFKL N702T under varied experimental conditions. (A-C) Time-lapse traces of the PFKL N702T assembly process at different protein and KCl concentrations. **(A)** At 20 mM KCl, PFKL N702T self-assembled into a single layer and then formed a second layer with reduced long-range order. At higher ionic strength, **(B)** 100 mM and **(C)** 300 mM, PFKL N702T predominantly self-assembled as a double-layer lattice. The lattice islands expanded laterally and fused to form a continuous, double-layered lattice. **(D)** Zoomed-in high-resolution images of PFKL N702T self-assembly at (i) 20 mM KCl and (ii) 100 mM KCl concentration. **(E)** 3D plot of surface coverage of PFKL N702T assemblies at different protein concentration, KCl concentration, and incubation time.

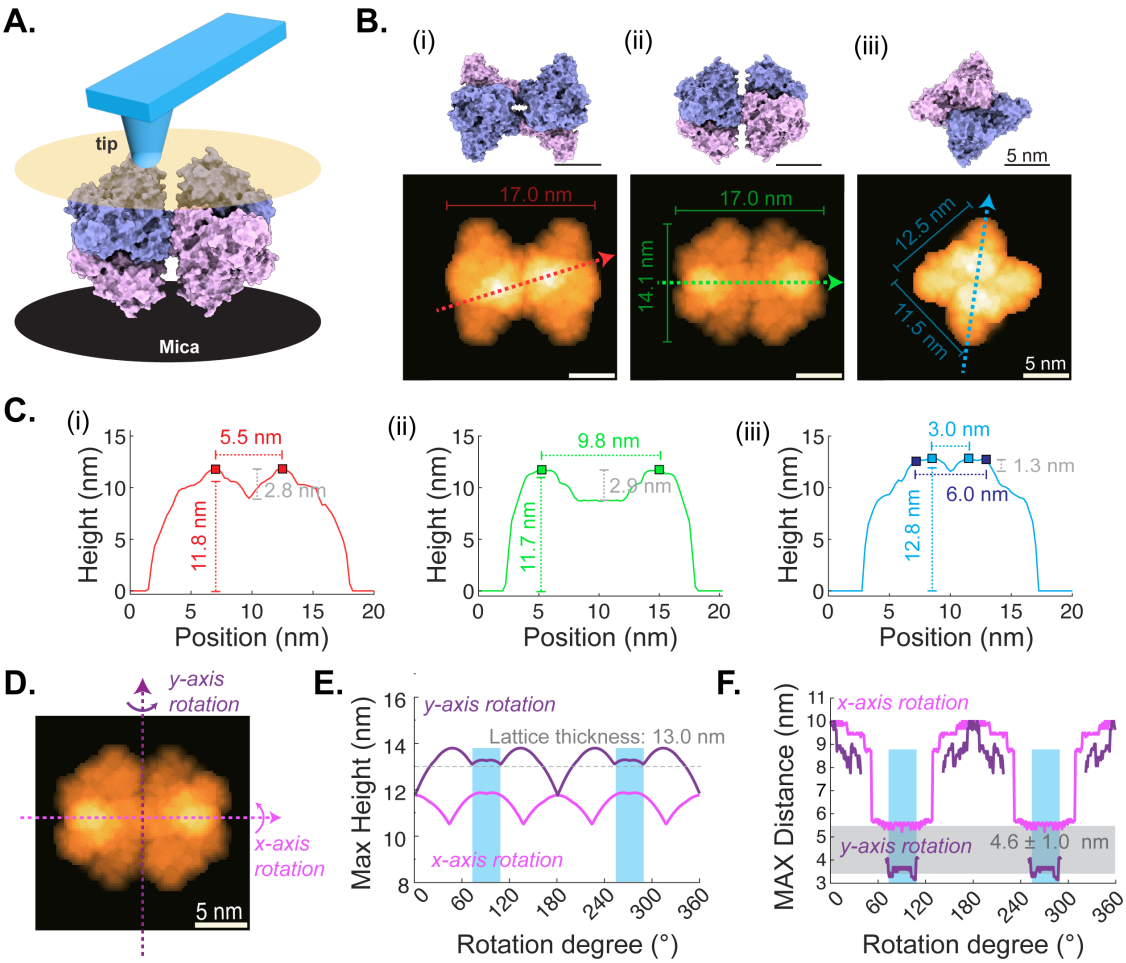

Figure S9. AFM image simulation defines PFKL N702T tetramer orientation within the lattice. (A) Simulated AFM imaging of the PFKL tetramer (PDB: 8W2G) using a computational probe with ~1.0 nm apex radius (15-degree tilt angle) to approximate HS-AFM tip convolution. **(B)** Simulated topographic projections of the tetramer from different orientations with labeled projected dimensions. **(C)** Representative cross-sectional profiles, extracted from (B), showing characteristic features, including protein height, distance between two protruding peaks, and peak-to-valley depth. **(D-F)** Systematic rotation of the tetramer along x- and y-axes and quantification of maximal height and peak separation. Experimental HS-AFM measurements (lattice thickness ~13.0 nm; peak spacing 4.6 ± 1.0 nm) match the simulated parameters of orientation (B-iii). In this configuration, the projected dimensions (~12.5 × 11.5 nm), thickness (~12.8 nm), peak spacing (~3-6 nm), and inter-peak depth (~1.3 nm) agree with lattice unit features observed in high-resolution HS-AFM images (**Fig. 5**).

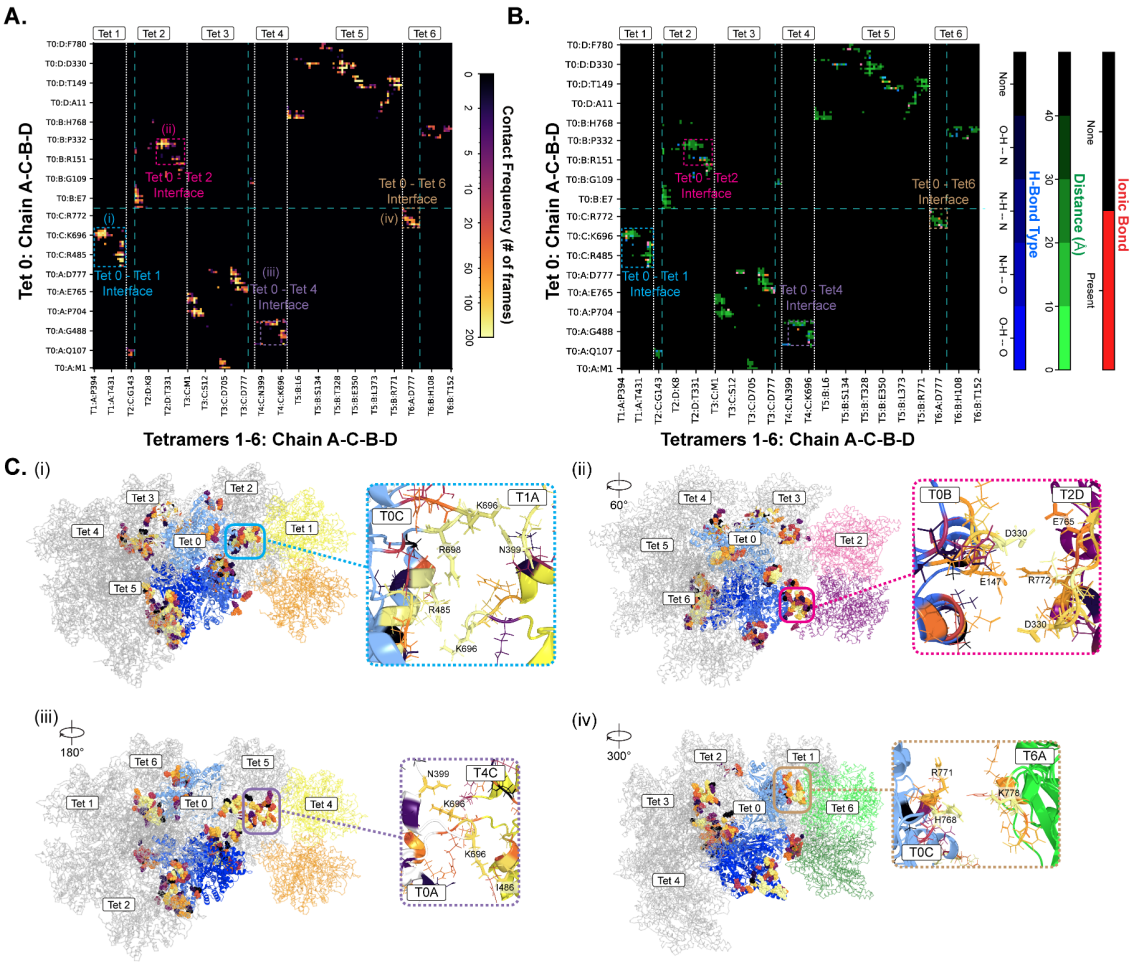

Figure S10. Inter-tetramer contacts in the PFKL N702T lattice. (A-B) Residue-residue contact maps showing **(A)** the frequency of inter-tetramer contacts observed during the 2-4 ns interval of the MD trajectory, with contacts defined by a Cβ-Cβ distance of 1.0 nm or less, and **(B)** a multichannel contact map of the inter-tetramer interaction network at 3 ns in the PFKL N702T lattice structure. The MD simulation trajectory is the same as that shown in **Fig. 6**. **(C)** Representative interfacial contacts at 3 ns in the PFKL N702T lattice structure, with residues making contacts colored according to contact frequency and shown as spheres. This panel shows additional representative inter-tetramer interfaces not highlighted in **Fig. 6E**.

252

Description of Supplementary Movies

Supplementary Movie 1. HS-AFM visualization of PFKL WT filament formation. PFKL WT (270-425 nM) was introduced into the HS-AFM liquid chamber containing buffer with 300 mM KCl. In the presence of 1 mM ATP and 2 mM F6P, PFKL WT assembles into filamentous structures with distinct geometries, including networked and linear filaments (related to **Fig. 2G**). Scale bar: 100 nm. Imaging parameters: 1 frame/s, 2 nm/pixel (networked filaments); 1 frame/s, 1 nm/pixel (linear filaments).

Supplementary Movie 2. APO-PFKL WT self-assembly on mica surfaces containing lipid membrane patches. HS-AFM imaging of PFKL WT assembly on mica surfaces containing pre-deposited lipid membrane patches (DOPC/DOPS, 60:40) in buffer with 100 mM KCl (related to **Fig. 3B**). PFKL WT at the indicated concentrations was introduced into the HS-AFM liquid chamber. At lower protein concentrations, PFKL WT primarily assembled into lattices on exposed mica surfaces. At higher concentrations, lattice assemblies extended across and over the lipid membrane patches. Scale bar: 100 nm. Imaging parameters: 1 frame/s, 1 nm/pixel.

Supplementary Movie 3. Edge dissociation of the PFKL N702T double-layer lattice. HS-AFM imaging of a PFKL N702T (100 nM) lattice assembled on freshly cleaved mica after 10 min incubation in buffer containing 100 mM KCl (related to **Fig. 4A**). During imaging, edge dissociation exposes the underlying second lattice layer. Scale bar: 30 nm. Imaging parameters: 1 frame/s, 0.5 nm/pixel.

Supplementary Movie 4. PFKL N702T self-assembles into a highly ordered 2D lattice at 100 mM KCl. PFKL N702T (300 nM) was added to the HS-AFM liquid chamber in buffer containing 100 mM KCl (related to **Fig. 4D**, left). During HS-AFM imaging, PFKL N702T molecules freely diffuse and deposit onto freshly cleaved mica for self-assembly. Scale bar: 100 nm. Imaging parameters: 1 frame/s, 1 nm/pixel.

Supplementary Movie 5. Self-assembly of PFKL N702T into an ordered 2D lattice at 300 mM KCl. PFKL N702T (300 nM) was introduced into the HS-AFM liquid chamber containing buffer with 300 mM KCl (related to **Fig. 4D & S8C**). During imaging, individual PFKL N702T molecules diffuse in solution, adsorb onto freshly cleaved mica, and progressively assemble into a highly ordered two-dimensional lattice. Scale bar: 100 nm. Imaging parameters: 1 frame/s, 1 nm/pixel.

Supplementary Movie 6. PFKL N702T assembly behavior at low ionic strength (20 mM KCl). PFKL N702T (300 nM) was introduced into the HS-AFM liquid chamber containing buffer with 20 mM KCl (related to **Fig. 4E**). During imaging, individual PFKL N702T molecules diffuse to the mica surface and initially form a single-layer assembly. Subsequently, a secondary layer stacks on top of the first layer. The resulting structures exhibit a more island-like morphology, distinct from the well-ordered double-layer lattices observed at higher KCl concentrations. Scale bar: 100 nm. Imaging parameters: 1 frame/s, 1 nm/pixel.

Supplementary Movie 7. High-resolution HS-AFM imaging of PFKL N702T lattices under different ligand conditions. PFKL N702T (100–200 nM) was introduced into the HS-AFM liquid chamber containing buffer with 300 mM KCl (related to **Fig. 5A**). Lattice formation was examined under APO, 1 mM ATP, and 1 mM ATP + 2 mM F6P conditions. Across these conditions, no significant differences in higher-order lattice organization were observed between ligand-free and ligand-bound states. Scale bar: 100 nm. Imaging parameters: 1 frame/s, 1 nm/pixel.

Supplementary Movie 8. High-resolution, zoomed-in HS-AFM imaging of PFKL N702T lattices under different ligand conditions. PFKL N702T (100-200 nM) was introduced into the HS-AFM liquid chamber containing buffer with 300 mM KCl (related to **Fig. 5B**). Lattice

structures were examined under APO, 1 mM ATP, and 1 mM ATP + 2 mM F6P conditions. At this higher magnification, individual lattice units are resolved, revealing intermolecular spacing and enabling analysis of tetramer orientation within the lattice. Scale bar: 10 nm. Imaging parameters: 0.6 frame/s, 0.33 nm/pixel (APO); 0.6 frame/s, 0.25 nm/pixel (ATP); 0.1 frame/s, 0.25 nm/pixel (ATP + F6P).

Supplementary Movie 9. Progressive dissociation of PFKL N702T from the center of a double-layer lattice. HS-AFM imaging of a highly ordered PFKL N702T two-dimensional lattice (100 nM) assembled on freshly cleaved mica after 10 min incubation in buffer containing 100 mM KCl (related to **Fig. 5E**). During imaging, individual PFKL N702T molecules gradually dissociate from the lattice center over time. Scale bar: 20 nm. Imaging parameters: 0.5 frame/s, 0.25 nm/pixel.

Supplementary Movie 10. MD simulation of PFKL N702T lattice. Representative video of MD simulation trajectory (2-4 ns) of the PFKL lattice, with front tetramers (Tet5 and Tet6) rendered transparent to highlight the packing geometry.